Research Article

Two different finite element models investigation of the plunge stage in joining AZ31B magnesium alloy with friction stir welding

Murat Turkan[1,2] · Özler Karakas[1]

Abstract

This study presents an investigation of the plunge stage in joining AZ31B magnesium alloy with friction stir welding using two different 3D finite element models based on Arbitrary Lagrangian–Eulerian formulation and Coupled Eulerian–Lagrangian formulation. The investigations are made with the ABAQUS program. Johnson–Cook plastic material law and Coulomb friction law are used in both models. Models are compared in terms of temperature, strain distribution, and processing time. In both models, very similar temperature and strain distributions are obtained in the weld zone and the models are validated by experimental results. In addition, with the increase in the rotational speed of the tool, temperature and strain in the welding zone increase similarly in both models. In the model using the Arbitrary Lagrangian–Eulerian formulation, mesh distortions occur when high mesh density is not created in the plunge zone. No problems related to mesh distortion are encountered in the model using Coupled Eulerian–Lagrangian formulation. Moreover, it is found that the model using the Coupled Eulerian–Lagrangian formulation has a lower processing time and this processing time is not affected by the rotational speed of the tool.

Keywords Friction stir welding · AZ31B magnesium alloy · Finite element model · Arbitrary Lagrangian–Eulerian formulation · Coupled Eulerian–Lagrangian formulation

1 Introduction

Friction stir welding (FSW) is a solid-state welding method developed at the welding institute (TWI) in Cambridge in 1991. In the conventional FSW process, a rotating tool consisting of pin and shoulder is used. This tool enters to material to be welded by turn around its own axis. It moves by rotating along the direction of the welding. Joining occurs without melting of material thanks to both friction and plastic deformation. Figure 1 represents the FSW process schematically.

During FSW, the material flow takes place in a very complex manner, depending on the welding parameters, tool geometry, and the properties of the material to be welded.

Figure 2 illustrates the metal flow around the axis of rotation of a threaded pin. First, owing to the friction of the tool shoulder, the metal under the shoulder flows towards the pin (movement 1), and then the material flows down along the surface of the pin (movement 2). After reaching the end of the metal pin, it flows backwards after a spiral path (movement 3) as demonstrated by the arrows in Fig. 2. By repeating the above three movements, the structure of the onion rings occurs in joint zone [2].

FSW has very important advantages over other welding methods. Perhaps the most important of these is the ability of this method to weld alloys which are very hard or impossible to join with conventional welding methods [3].

✉ Özler Karakas, okarakas@pau.edu.tr | ¹Department of Mechanical Engineering, Faculty of Engineering, Pamukkale University, 20160 Kinikli, Denizli, Turkey. ²Department of Mechanical Engineering, Faculty of Engineering, Izmir University of Economics, 35330 Balcova, Izmir, Turkey.
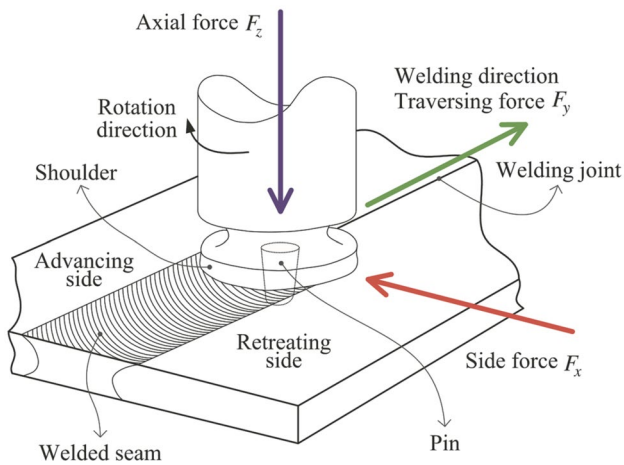
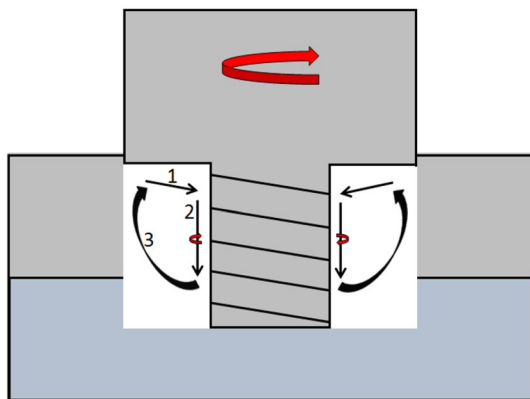**Fig. 1** Schematic demonstration of the FSW process [1]

Fig. 2 Schematic representation of the material flow in the FSW process [2]

Numerical simulation of FSW is an effective method to predict the defects that may occur during the process and to optimize the number of experiments in terms of time and cost [4]. Moreover, modeling of FSW with finite element method is of great importance in terms of analyzing the material behavior in detail during the process.

FSW is a thermo-mechanical process and equations of a thermo-mechanical process can be conventionally expressed in two different formulations. These are Lagrangian and Eulerian formulations. In the Lagrangian formulation, the mesh is at the material points, and in the Eulerian formulation the mesh is at the spatial points. In the Lagrangian formulation, the mesh moves during the material flow and follows the material points. In the Eulerian formulation, mesh is fixed. The method that combines the advantages of these two formulations is referred to as the Arbitrary Lagrangian–Eulerian (ALE) method. In the last two decades, ALE, an efficient and adaptable method,

has been used to analyze highly interactive problems [5]. When the literature is examined, there are studies involving modeling of the FSW using the ALE formulation [6–8]. ALE method and adaptive meshing are commonly utilized to prevent mesh distortion. ALE adaptive mesh permits the mesh to move independently of the material [6]. Even if ALE allows the material to behave arbitrarily and complex, it cannot precisely prevent remeshing. Therefore, ALE is suitable for analyzing at local level, such as stirring zone [9].

Coupled Eulerian–Lagrangian (CEL) formulation is frequently used to modeling the excessive plastic deformation in the FSW process. The CEL formulation divides the whole control volume into Eulerian and Lagrangian domains and it overcomes the challenges of frictional modeling in computational fluid mechanics and massive deformation in computational solid mechanics [10]. Recently, studies involving modeling of FSW with CEL formulation have been conducted [4, 11, 12]. During the CEL analysis, Lagrangian mesh interacts with materials in the Eulerian portion. This technique is suitable for modeling material flow. Moreover, defect formation can be observed in models using CEL formulation [4, 12, 13]. In a study, a comparison of these two methods was done for orthogonal cutting and it is stated that mesh distortions occur in the ALE model [14].

When the studies in the literature are examined, it is seen that FSW has modeled using either the ALE formulation or the CEL formulation. Unlike the aforementioned citations, in this research a detailed comparison was made between these two formulations for AZ31B magnesium alloy using same material properties and process parameters. Temperature distribution, strain distribution and process time have been examined in detail for these two formulations.

This article is organized as follows. In Sect. 2, information about geometry of models and mesh properties, material model, boundary conditions is given. In Sect. 3, the experimental study is detailed. In Sect. 4, mass scaling is verified, and two models are compared in terms of temperature distribution, plastic strain distribution and processing time. Finally, in Sect. 5, a summary of experimental results is presented and recommendations for future studies are proposed.

2 Numerical method

2.1 Geometry of models and mesh properties

In this study, the plunge stage of FSW was investigated with the ABAQUS program with two different models using the ALE formulation and the CEL formulation. The

Fig. 3 Dimensions of the used tool in the models
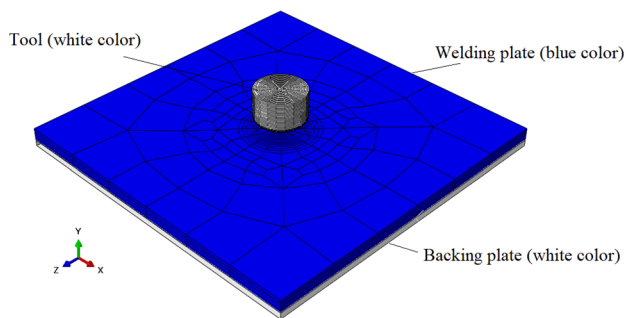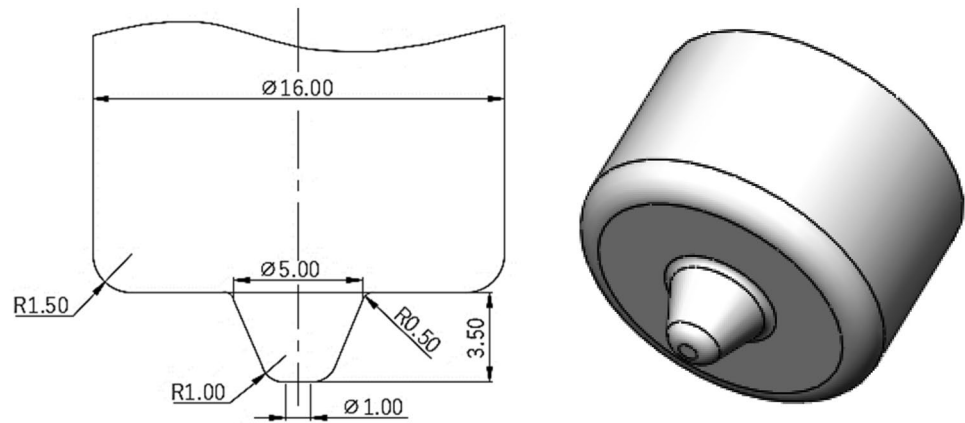
Fig. 4 Model using the ALE formulation
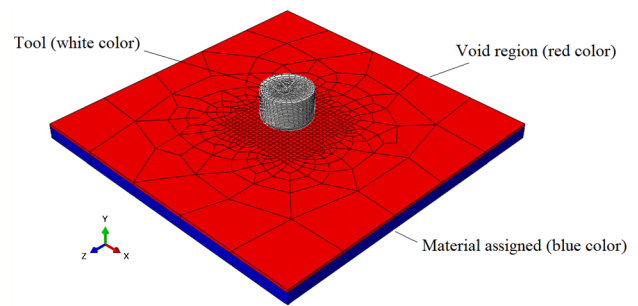
Fig. 5 Model using the CEL formulation

adaptive meshing method in the ABAQUS program integrates the properties of pure Lagrangian analysis and pure Eulerian analysis. Analysis with this adaptive meshing type is often called the ALE analysis. ALE adaptive mesh allows the mesh to move freely of the material, allowing a high-quality mesh to be created from beginning to end an analysis even if there are major deformations or material losses. Adaptive mesh only moves nodes, but mesh topology remains unchanged [15]. The model using the ALE formulation composes of a deformable Lagrangian workpiece, a rigid Lagrangian tool and a rigid Lagrangian support plate. The workpiece in the model using ALE formulation is 4 mm thick and has 100 mm side lengths. The C3D8RT element type has used to mesh the workpiece. There are 3969 nodes and 3440 elements in the work piece used the ALE formulation. A higher mesh density has been created in the plunge region of the pin to provide more realistic outputs and to prevent excessive mesh distortions. The dimensions of the used tool in both models are shown in Fig. 3 and the model using the ALE formulation is demonstrated in Fig. 4.

In models that include both Eulerian piece samples and Lagrangian piece samples, analysis is often referred to as the CEL analysis. During the CEL analysis, Lagrangian mesh contacts with materials in the Eulerian portion [15]. In the model using the CEL formulation, the workpiece was formed as a Eulerian body, while the tool was formed as a rigid Lagrangian body. The workpiece with EC3D8RT element type has used. There are 4146 nodes and 3400 elements in the workpiece used in the CEL formulation. The workpiece is divided into two areas to identify the void region and the material assigned area as shown in Fig. 5. No material properties have been given in the void region. Creating the void region in model using the CEL formulation is necessary to observe the flash formation that frequently occurs during FSW. The thickness of the void region (colored in red) is 1 mm and the thickness of the region (colored in blue) assigned to the material is 4 mm. The workpiece has side lengths of 100 mm. Abaqus program offers the option to remove the pre-determined void part at the end of the CEL analysis. Only when this void is removed, the deformation in the CEL analysis can be seen on the whole model as in the ALE analysis. Therefore, in the model in which the CEL formulation is used, the material assigned to the area is 4 mm and the void region is 1 mm. In this way when the void region is removed, the deformation will appear just like in ALE analysis. In the model using ALE formulation, the workpiece is 4 mm.

2.2 Material model

During FSW, high strain rates and temperatures are achieved in the workpiece. Numerical modeling of FSW involves difficulties due to nonlinear material behavior in the process [4, 8]. To solve this complex problem, the Johnson–Cook material law, which depends on the temperature and strain rate, was used. With the Johnson–Cook plastic material law, σ yield stress is found by Eq. (1).

$$\sigma = \left[A + B\left(\varepsilon_P\right)^n \right]\left[1 + Cln\left(\frac{\dot{\varepsilon}_P}{\dot{\varepsilon}_0}\right) \right]\left[1 - \left(\frac{T - T_{room}}{T_{melt} - T_{room}}\right)^m \right] \tag{1}$$

In Eq. (1); ε_p and $\dot{\varepsilon}_p$ are the equivalent plastic strain and plastic strain rate respectively. $\dot{\varepsilon}_0$ is the reference strain rate, T refers to reference temperature, T_{melt} denotes melting temperature of the material and T_{room} is the ambient temperature. A, B, C, n and m are constants depending on the material properties. In this study; $\dot{\varepsilon}_0 = 0.001$ [16], $T_{room} = 20$ °C, $T_{melt} = 630$ °C. Other constants used for the AZ31B alloy are shown in Table 1.

2.3 Thermal model

The general heat source in the FSW process is the energy generated by the friction between the tool and the workpiece surfaces and the slip deformation around the tool. The heat transfer in the plunge stage of the FSW process can be expressed by Eq. (2) [18].

$$\rho c \frac{\partial T}{\partial t} = \frac{\partial}{\partial_x}\left[k_x \frac{\partial T}{\partial x} \right] + \frac{\partial}{\partial_y}\left[k_y \frac{\partial T}{\partial y} \right] + \frac{\partial}{\partial_z}\left[k_z \frac{\partial T}{\partial z} \right] + \dot{q}_p \tag{2}$$

In Eq. (2); ρ is the density, c is the specific heat, k denotes the heat transfer coefficient, T is the temperature, t refers to time and x, y, z are the spatial coordinates. $\dot{q}_p$ is the heat of the plastic energy-induced generated by shear deformation. $\dot{q}_p$ is calculated by Eq. (3).

$$\dot{q}_p = \eta\sigma\dot{\varepsilon}^{pl} \tag{3}$$

Here; η is the constant that determines the conversion of plastic energy to temperature and its value equal to

0.9 [19] was taken in this study. σ is the shear stress and $\dot{\varepsilon}^{pl}$ is the plastic strain rate.

In the FSW process, the surface heat flux is calculated by Eq. (4) [20].

$$Heat\ flux(Q) = \frac{Heat\ input(q)}{Area(A)} \tag{4}$$

The area here is calculated by Eq. (5) as follows,

$$A = \pi(R - r)^2 \tag{5}$$

In Eq. (5), R is the shoulder radius and r is the pin radius.

Heat input (q) can be calculated with the Frigaard equation [21] as in Eq. (6).

$$Heat\ input(q) = \int_0^R 2\pi\mu\omega Pr^2 dr \tag{6}$$

Here, ω is the angular velocity of the tool and it is calculated by Eq. (7) as,

$$\omega = 2\pi n / 60 \tag{7}$$

where n is the number of revolutions, P is the stress and obtained by Eq. (8).

$$P = F / A \tag{8}$$

In Eq. (8), F is the axial force.

As a result, the heat generated by friction between the tool and workpiece is obtained by Eq. (9) [22].

$$\dot{q}_f = \frac{4}{3}\pi^2\mu PnR^3 \tag{9}$$

Thermal and mechanical properties depending on the temperature used in the models are listed in Table 2.

2.4 Boundary conditions

Since the workpiece is a Lagrangian body in the model using the ALE formulation, the side surfaces and the bottom surface of the workpiece were defined as encastre surface. In the model using the CEL formulation, the velocity was equalized to zero on all surfaces of the workpiece using the control volume approach. The boundary conditions in the models are shown in Fig. 6. In the model using the ALE formulation, the workpiece top surface and tool were modeled as the slave surface and master surface respectively. Surface to surface contact relation was given, and penalty contact method was applied. In the model using the CEL formulation, general contact conditions were applied. Friction coefficient selection is important in terms of heat generation. Friction coefficient largely depends on the temperature. Depending on the temperature, the friction coefficients used in both models are given in Table 3. Heat transfer from

Table 1 Constants used in the Johnson–Cook plastic material model [17]

A (MPa)	B (MPa)	C	n	m
224	380	0.02	0.76	1.55

Table 2 Thermal and mechanical properties depending on the temperature used in the models

Material	Modulus of elasticity [23, 24]		Thermal conductivity [25]		Specific heat [25]		Thermal expansion coefficient [25]	
	T (°C)	E (GPa)	T (°C)	k (W/m K)	T (°C)	C_p (J/kg K)	T (°C)	α (K^{-1})
AZ31B	27	45	20	96.4	20	1050	20	7.7E−006
	102	43	100	101	100	1130	150	2.64E−006
	202	41	200	105	200	1170	300	2.7E−006
	297	38	250	107	300	1210	400	2.7E−006
	342	37	300	109	350	1260	550	2.95E−006
	397	35.5	400	113	400	1300		
	424	34.5	420	114	450	1340		
	578	15	440	115	470	1340		
	608	1	460	116	500	1360		
	632	0						

Fig. 6 Boundary conditions **a** ALE, **b** CEL

(a)

(b)
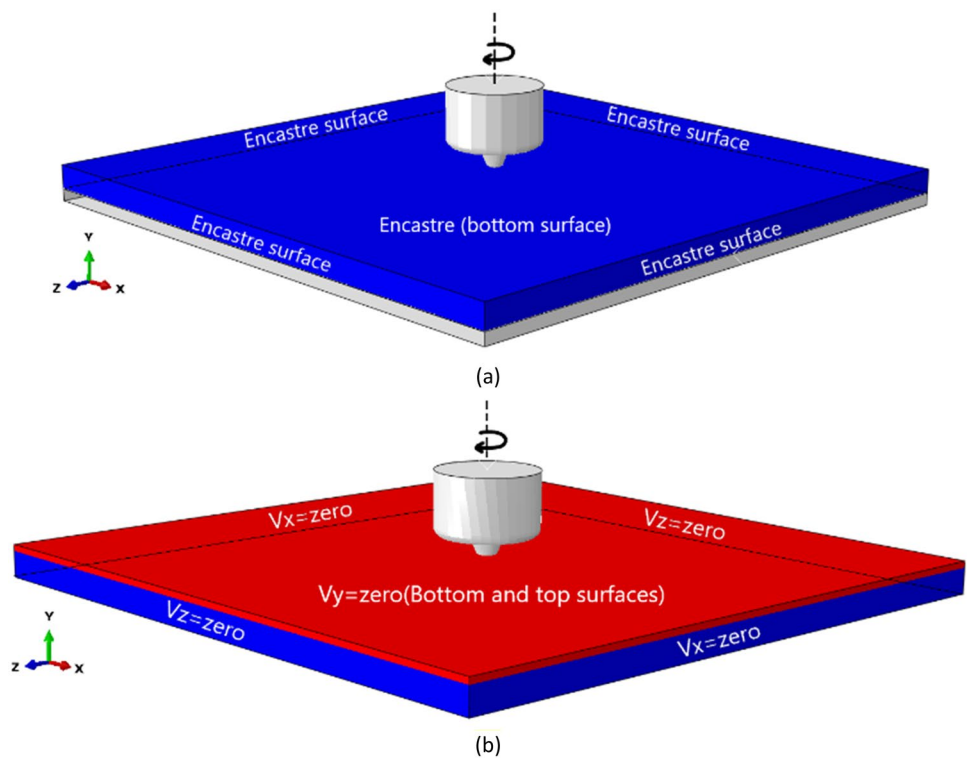
Table 3 Temperature dependent friction coefficients used in models [27]

Temperature (°C)	Friction coefficient
25	0.30
300	0.25
420	0.20
543	0.01

the lower surface of the workpieces, were controlled heat transfer coefficient of 2000 W/m^2 K and heat transfer from the upper surface of the workpieces were controlled with a heat transfer coefficient of 10 W/m^2 K [26]. In the models, the tool was rotated at three different speeds as 200, 300 and 400 rpm. In both models, the tool was dived 3.6 mm into workpiece at a constant speed in 15 s. Since the length of the pin is 3.5 mm, the plunge depth is 0.1 mm.

3 Experimental study

Experimental studies have been carried out with AZ31B magnesium plates of 100×100×5 mm dimensions. A CNC milling machine was used for experimental studies. A tool

of the same dimensions used in the numerical models was produced and its hardness was increased by heat treatment. The tool obtained by machining from 42CrMo4 steel was kept in the heat treatment furnace at 840 °C for 30 min and then cooling was given in oil. After cooling, a hardness of 47 HRC was reached on the outer surface. The temperature was measured during the process, depending on the time, at a distance of 14 mm from the welding center with a K type thermocouple (see Fig. 7). The photographs of the surface after welding and the 3 mm deep and 5 mm diameter holes where the temperature was measured are shown in Fig. 8.

4 Results and discussion

4.1 Verifying mass scaling

Mass scaling method can be utilized to minimize simulation time [28]. In this study, mass scaling method was used. In one study, it has been stated that if the mass scaling factor is 10^6 in FSW, an acceptable temperature area can be calculated in less processing time [29]. In addition, in
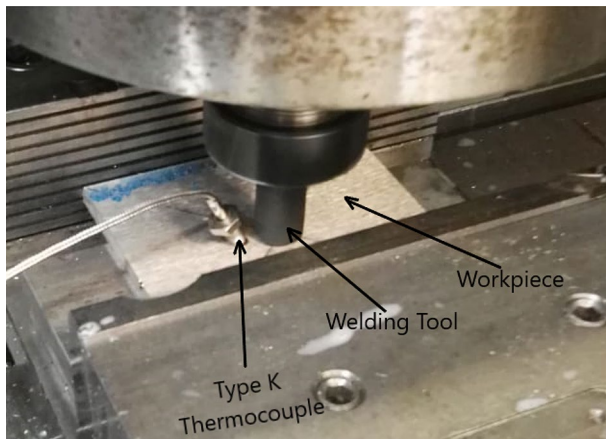
Fig. 7 Performing the plunge process with CNC milling machine
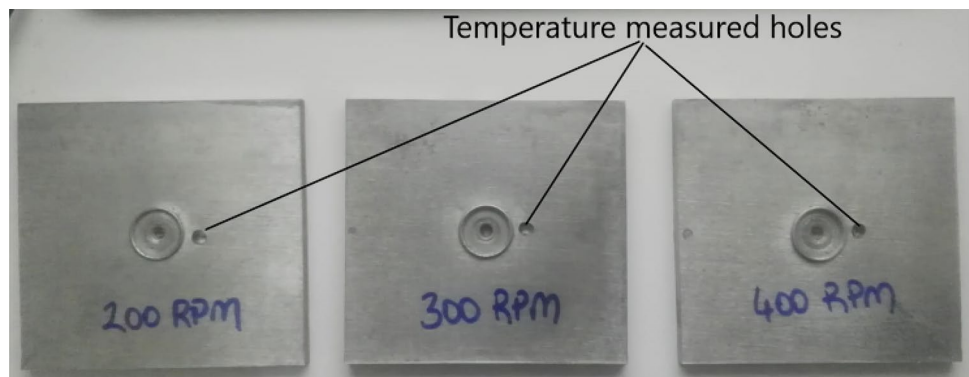
another study, the mass scaling method was successfully used to develop the CEL formulation in the simulation of the forming process [30]. The ratio of kinetic energy and internal energy must be less than 1% in order for the simulation results made by mass scaling to be evaluated as a reasonable estimate [11]. In model using the ALE formulation, when the mass scaling factor is 10^5, the ratios of kinetic energy and internal energy are shown in Figs. 9, 10 and 11. The maximum rate is 0.164. Therefore, it can be concluded that mass scaling has minor effect on the results obtained.

4.2 Temperature distribution

FSW is a thermo-mechanical process and it is known that thermo-mechanical processes significantly develop the mechanical properties of magnesium and its alloys [31]. Moreover a reasonable level of heat input is beneficial for plastic deformation that determines the formation and strength of the joint [32, 33]. During FSW, the temperature in the stirring zone reaches 0.6 to 0.9 times the melting point of the matal to be welded [34]. As well as defects from excessive heat input, defects may occur due to low heat input [35]. Therefore, it is important to examine the welding-zone temperature distributions. Welding-zone temperature distributions are illustrated in Figs. 12, 13, 14, 15, 16 and 17 for both models. It is observed that the temperature distributions are similar in both models and the temperature increases with increasing rotational speed of the tool.

In the models, reference points have been determined for observing the change of temperature with respect to time. These reference points are shown in Fig. 18. In the model using the ALE formulation, initially the reference point is 14.6 mm away from the welding center and it has moved towards the welding center during the process (Fig. 19). In the model using the CEL formulation, the reason for not placing the reference point on the top surface of the workpiece is that no material is assigned to the top surface of the model. In the model using the

Fig. 8 After the process top surface appearances and temperature measured holes

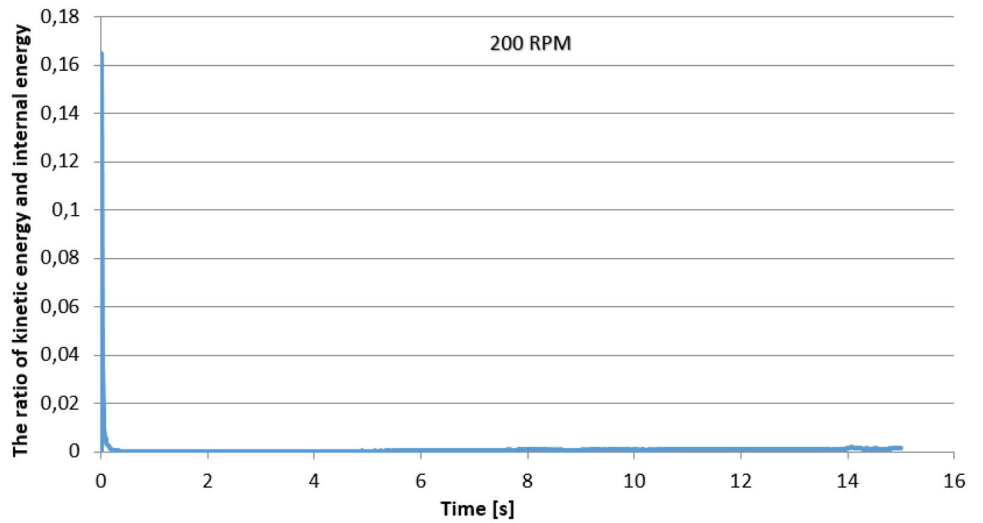**Fig. 9** The ratio of kinetic energy and internal energy at 200 rpm tool rotation speed

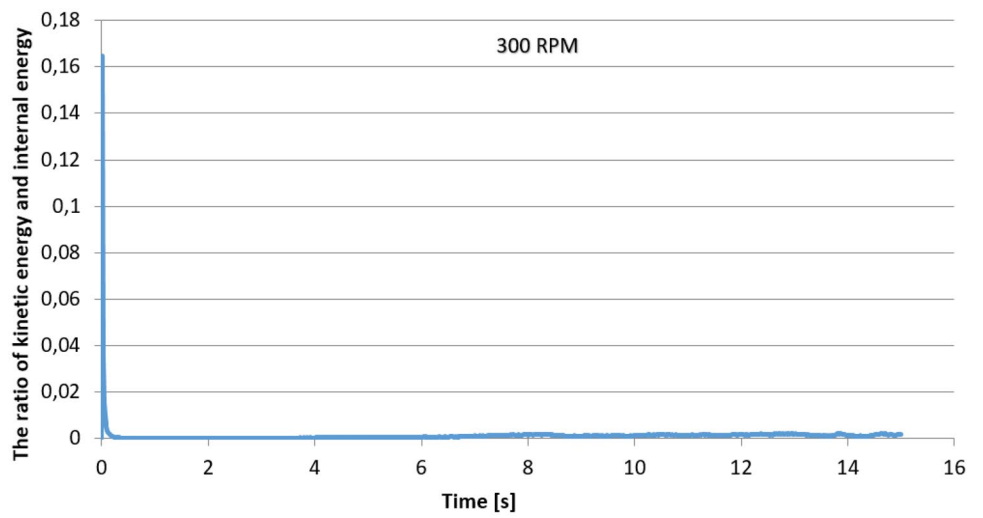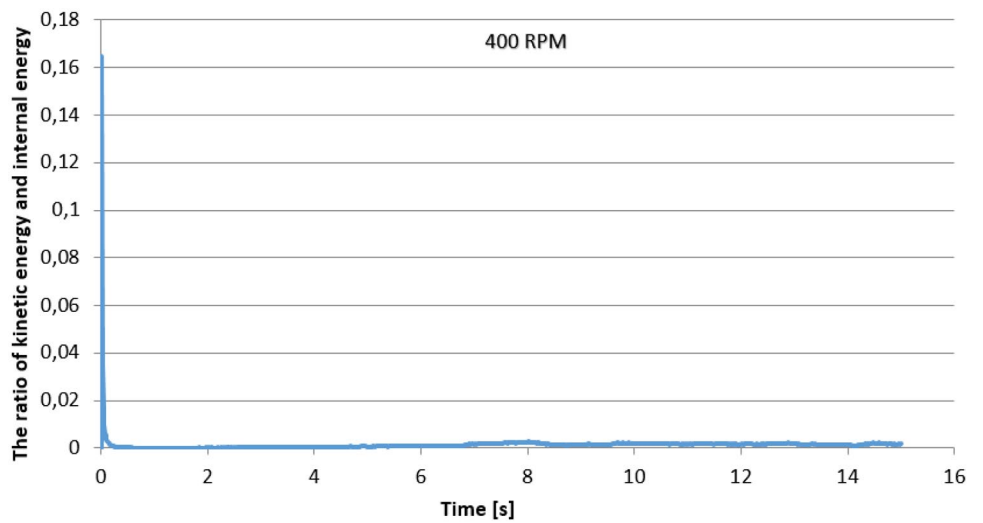**Fig. 10** The ratio of kinetic energy and internal energy at 300 rpm tool rotation speed

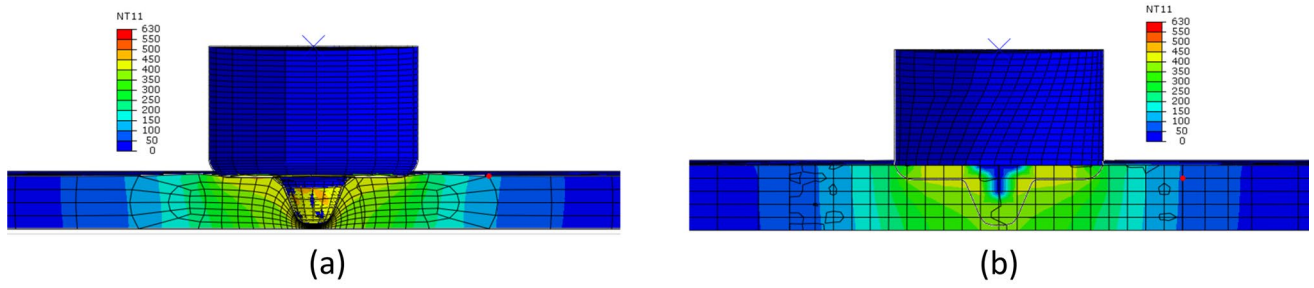**Fig. 11** The ratio of kinetic energy and internal energy at 400 rpm tool rotation speed

Fig. 12 Temperature distributions at the end of step in cross section at 200 rpm **a** ALE, **b** CEL
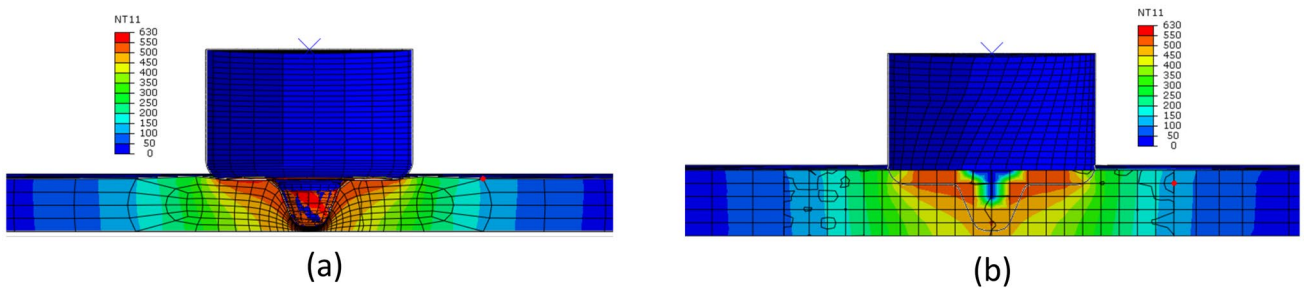

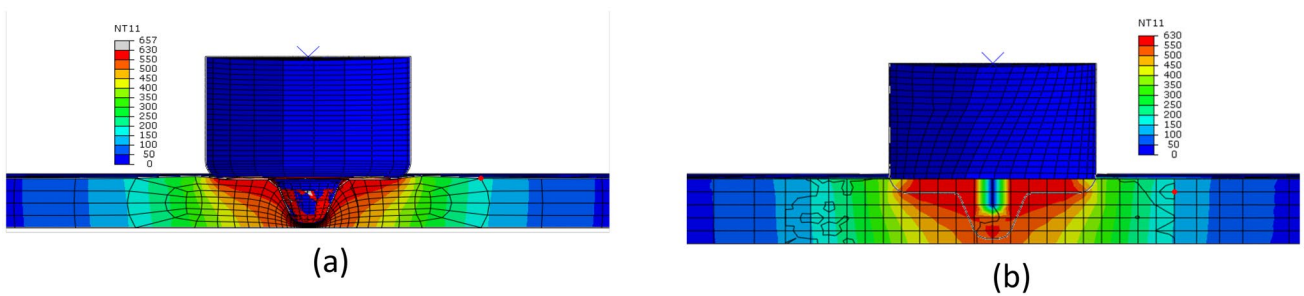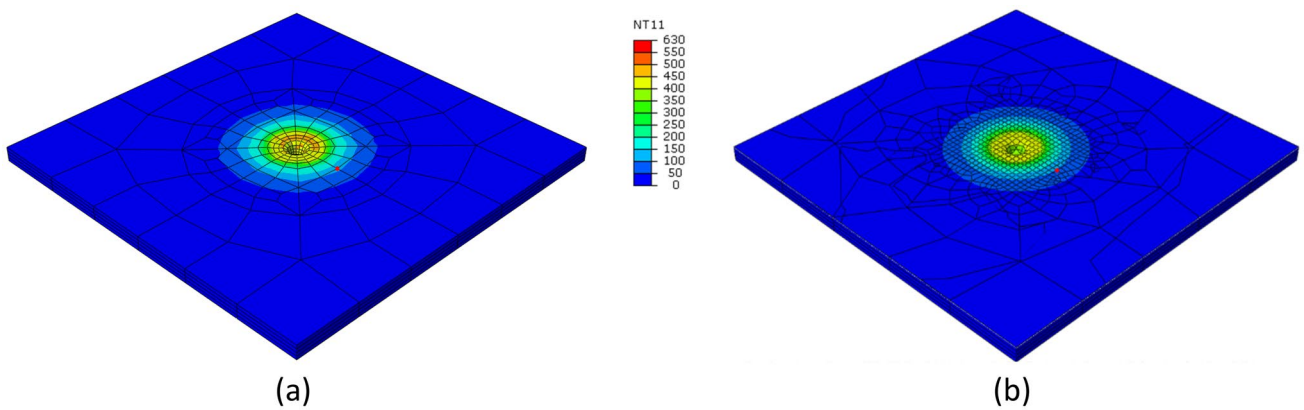**Fig. 13** Temperature distributions at the end of step in cross section at 300 rpm **a** ALE, **b** CEL

Fig. 14 Temperature distributions at the end of step in cross section at 400 rpm **a** ALE, **b** CEL

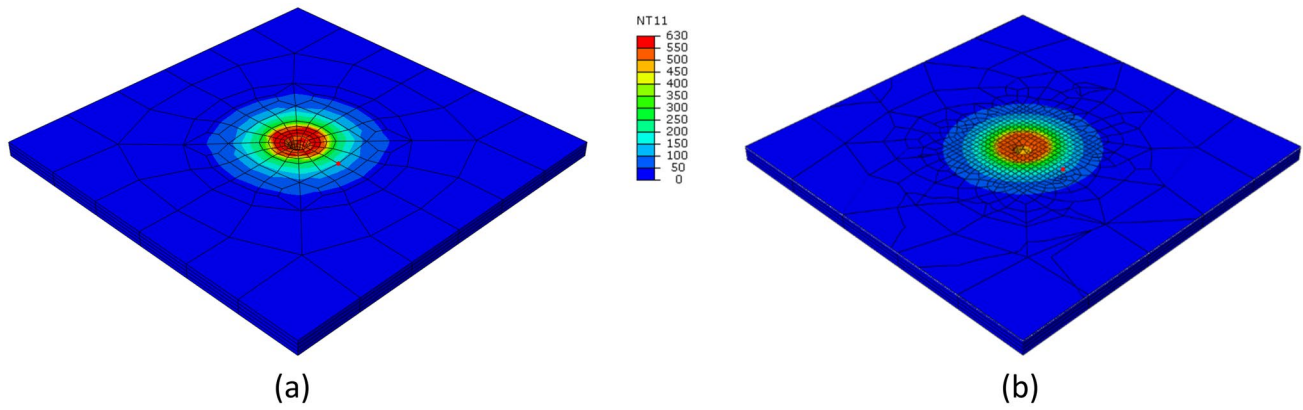**Fig. 15** Temperature distributions at the end of the step at the top surface at 200 rpm **a** ALE, **b** CEL

Fig. 16 Temperature distributions at the end of the step at the top surface at 300 rpm **a** ALE, **b** CEL
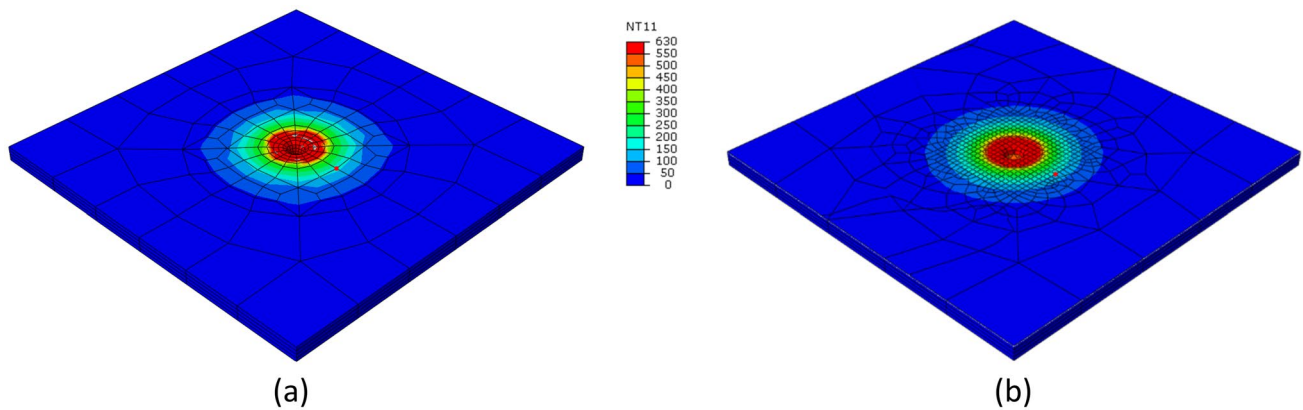

Fig. 17 Temperature distributions at the end of the step at the top surface at 400 rpm **a** ALE, **b** CEL
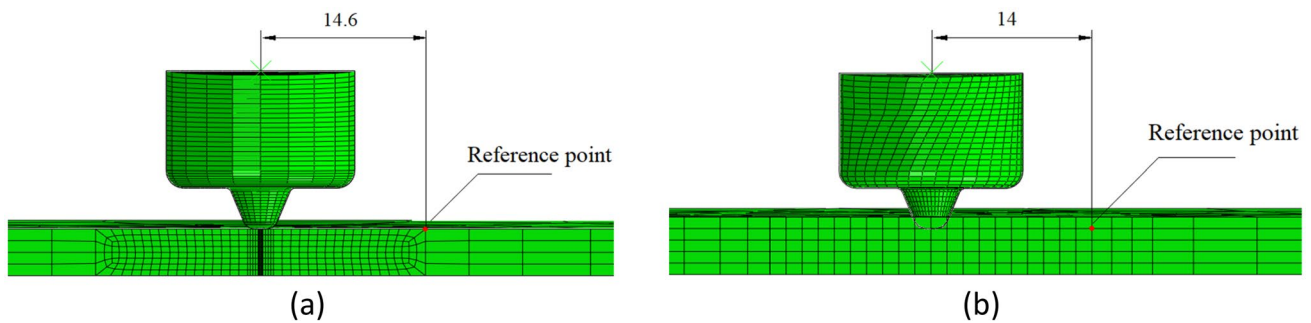

Fig. 18 Locations of the points where temperature measurement is held **a** ALE, **b** CEL

CEL formulation, no significant change of coordinates was observed during the process at the reference point, which was initially 14 mm away from welding center.

Diagrams of temperature change at the reference points of the models are shown in Fig. 20 and the comparison of the temperature at the reference point of both models is shown in Fig. 21. When the tool's rotation speed increases, the temperature at the reference point increased greatly especially after the contact of the tool shoulder. It is known that the tool shoulder importantly affects the movement of material at the top of the joint [36]. In addition, the diameter of the tool shoulder is very significant because it provides the formation of a large part of the heat required during FSW [37–39]. Similar
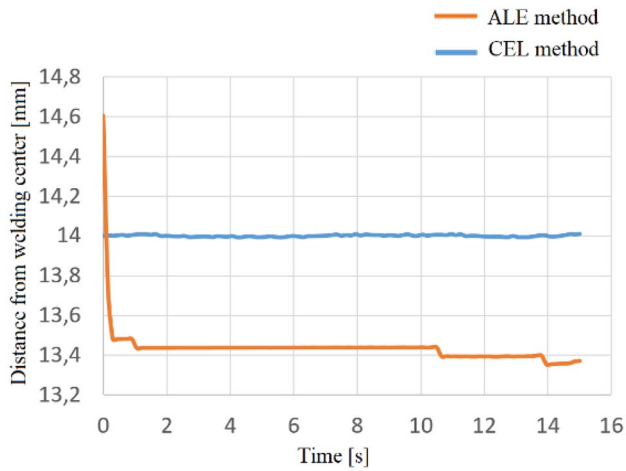
Fig. 19 Distance to the welding center of the points where the temperature is measured

temperature distributions were observed at the reference points of both models with respect to time. There is similarity between the temperature distributions in the two models and the temperature distributions obtained from the experimental study. Numerical models were verified by experimental temperature data at 14 mm from the welding center. In the experimental study, slightly lower top temperature was obtained from both models. In this case, material behavior in numerical models may

have an effect. In addition, a slightly softer temperature increase was observed in the experimental study. In the model using the ALE formulation, the temperature was measured higher since the point where the temperature was measured moves towards the welding center during the process. In the model using the CEL formulation, the reference point is constantly 14 mm away from the welding center during the process. In the model using the ALE formulation, the distance of the reference point to welding center, which was initially 14.6 mm, was 13.37 mm at the end of the process. Moreover in the model using the CEL formulation, the workpiece behaves 1 mm thicker during operation due to void region. With thicker workpiece, the area where heat spreads will increase.This difference in thickness is an another factor in measuring lower temperatures in the model using the CEL formulation compared to the model using the ALE formulation.

4.3 Plastic strain distribution

Equivalent plastic strain (PEEQ) value is a variable used to observe the inelastic behavior of the material. PEEQ value is the integrated measure of the plastic strain. When this value is greater than zero, yielding occurs in the material [15]. PEEQ distributions at the end of step are shown in Figs. 22, 23 and 24. When the tool's rotation speed increases, the PEEQ values at the welding region have increased substantially. In general, PEEQ distributions are
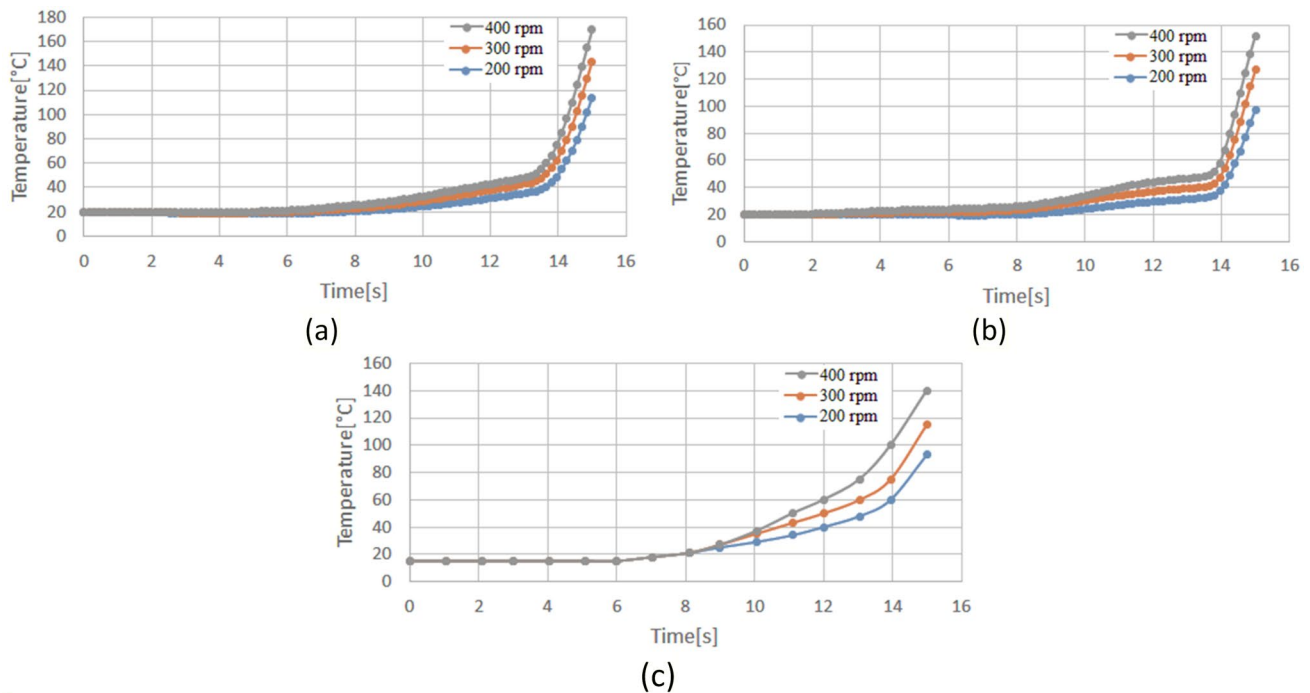

Fig. 20 Temperature at the reference point with respect to time **a** ALE, **b** CEL, **c** experimental
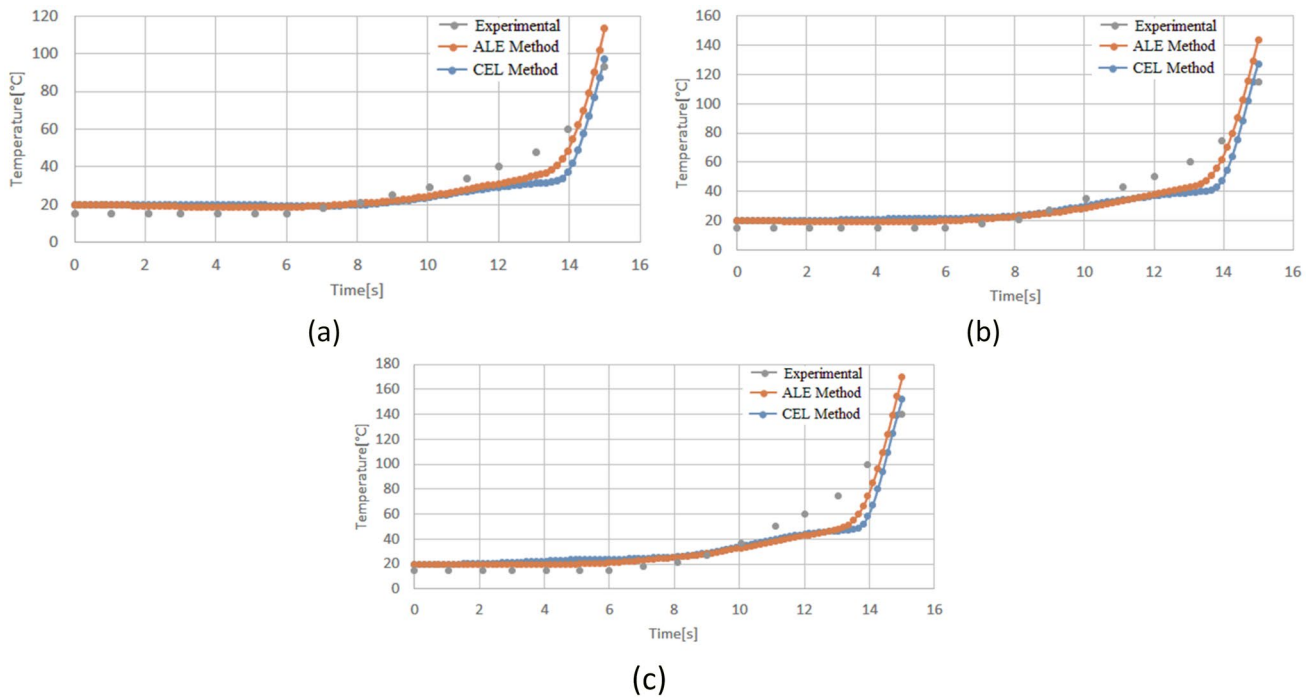
(a)

(b)

(c)

Fig. 21 Comparison of the temperature at the reference point **a** 200 rpm, **b** 300 rpm, **c** 400 rpm

(a)

(b)

Fig. 22 PEEQ distributions at the end of the step at 200 rpm **a** ALE, **b** CEL
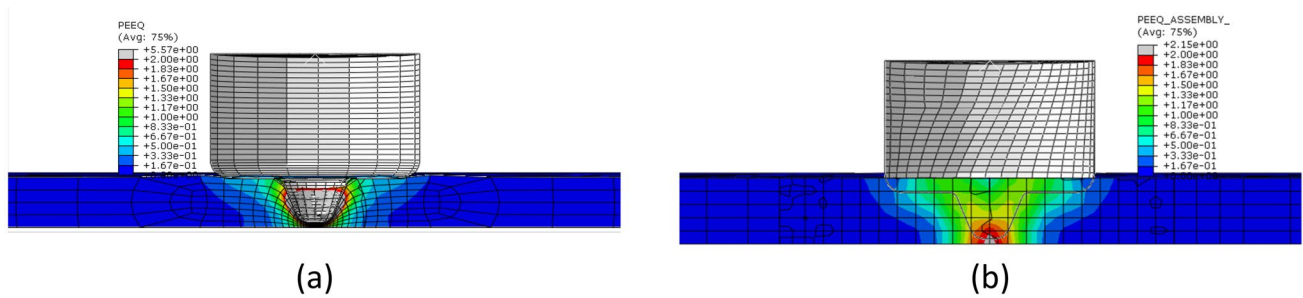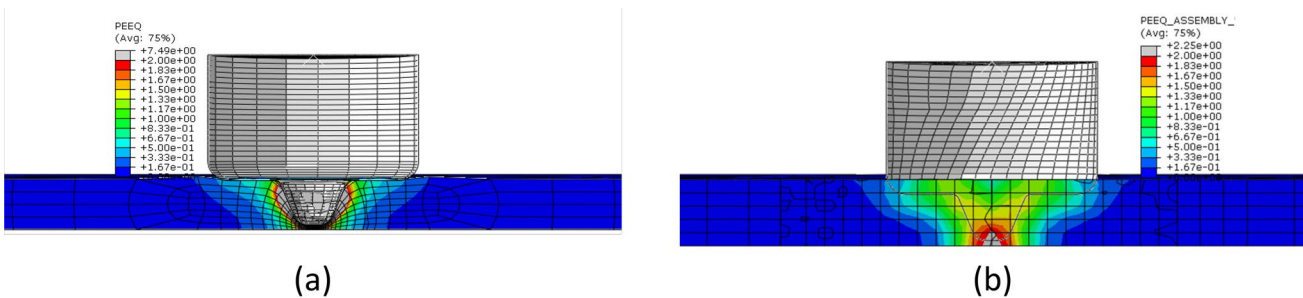

(a)

(b)

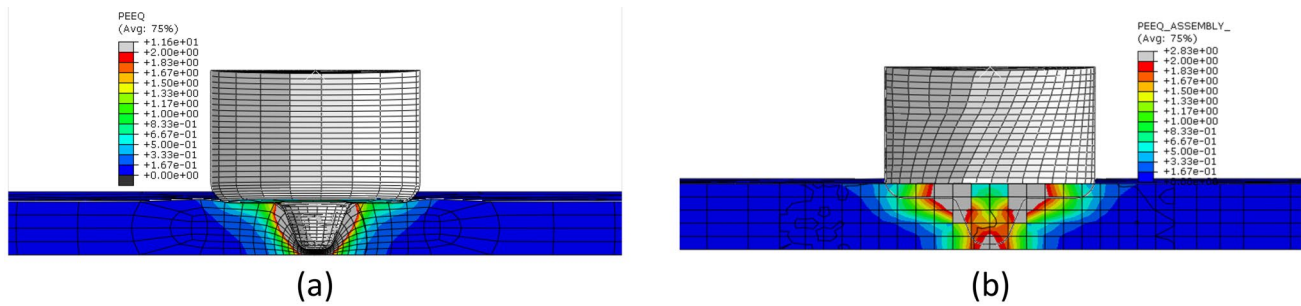**Fig. 23** PEEQ distributions at the end of the step at 300 rpm **a** ALE, **b** CEL

Fig. 24 PEEQ distributions at the end of the step at 400 rpm **a** ALE, **b** CEL
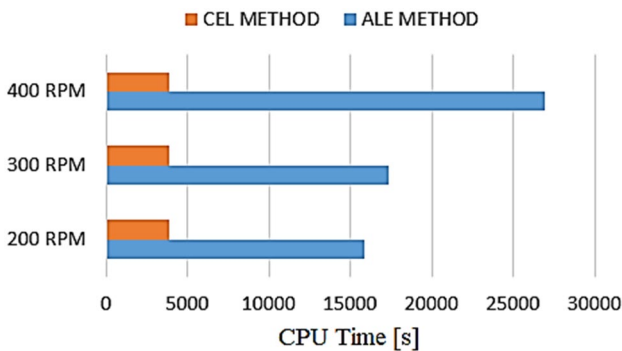

Fig. 25 Comparison of the CPU time

similar in both models. In the model using the ALE formulation, PEEQ values was higher on the contact surfaces due to the surface to surface (penalty) contact method. In the model using the CEL formulation, although strain values are lower on the contact surfaces, it is observed that the strain is distributed over a larger area. It is obvious that the contact method and coarse mesh have an effect on the occurrence of this situation. While surface to surface contact (penalty) relation was given in the model using the ALE formulation, general contact relation were applied in the model using the CEL formulation.

4.4 Processing time

Although the number of elements and nodes are approximately equal, the model using the ALE formulation has a higher processing time (see Fig. 25). Even though there is no significant change in the processing time with the increase in the rotational speed in the model using the CEL formulation, the processing time has increased with the increase in the rotational speed in the model using the ALE formulation. In this case, the contact method is thought to have an effect. In addition, the requirement to create a high mesh density in the plunge region of the pin was effective in the higher processing time in the model with ALE. In the model using the ALE formulation, higher

mesh density has been created in the plunge zone since it has observed that mesh distortions occur when high mesh density is not created in the plunge zone. In the model using CEL formulation, no problem was observed with regard to mesh density during the process. In addition, it was observed that the process could not proceed at a tool rotation speed higher than 400 rpm in the model using ALE formulation. In the model using the ALE formulation, it is necessary to create a much higher mesh density in the plunge zone in order to analyze at rotational speeds higher than 400 rpm. Since this would extend the process time much more, investigations were made at 200, 300 and 400 rpm.

5 Conclusions

The plunge stage in joining of AZ31B magnesium alloy with FSW has been successfully modeled with two different models using ALE and CEL formulations. Very similar temperature and strain distributions at the welding region have observed in these models. The models are validated by experimental results. In both models, when the tool's rotation speed increases, the temperature in the welding region has increased similarly. Moreover, the tool shoulder has a greater effect than the pin in terms of heat input. In the model using ALE formulation, when high mesh density has not created in the plunge region of the pin, mesh distortions have occurred. Therefore, in the model using the ALE formulation, a higher mesh density has been created in the plunge region. In the model using CEL formulation, no problem has observed related to the mesh density. The CPU time is higher in the model using the ALE formulation. In addition, when the tool's rotation speed increases in the model with ALE formulation, the CPU time has dramatically increased. However, in the model with CEL formulation the CPU time is independent of the tool rotational speed. The CEL formulation may be more preferable to FSW modeling than the ALE formulation because no mesh distorsion occur in this formulation and it has a shorter

processing time. Moreover, when the mass scaling factor is 10^5 in FSW, a reasonable temperature distribution can be obtained with less calculation time. In this study, analyzes were carried out at 200–300–400 rpm tool rotational speeds and 15 s plunging time. It should be kept in mind that results may vary at different tool rotational speeds and plunging times. In addition, mass scaling technique was applied to reduce the simulation time in this study. Higher temperatures may have been observed on the contact faces due to the mass scaling technique. Moreover, using different material properties in models may change the results. As a continuation of this study, the plunge stage can be analyzed with different tool geometries or the whole process can be investigated. Lastly, material flow characteristics during the process can be examined with models using CEL formulation.

Compliance with ethical standards

Conflict of interest The authors declare no conflict of interest.

References

1. Mendes N, Loureiro A, Martins C et al (2014) Effect of friction stir welding parameters on morphology and strength of acrylonitrile butadiene styrene plate welds. Mater Des 58:457–464. https://doi.org/10.1016/j.matdes.2014.02.036
2. Li Y, Qin F, Liu C, Wu Z (2017) A review: effect of friction stir welding on microstructure and mechanical properties of magnesium alloys. Metals 7:524. https://doi.org/10.3390/met7120524
3. Gibson BT, Lammlein DH, Prater TJ et al (2014) Friction stir welding: process, automation, and control. J Manuf Process 16:56–73. https://doi.org/10.1016/j.jmapro.2013.04.002
4. Chauhan P, Jain R, Pal SK, Singh SB (2018) Modeling of defects in friction stir welding using coupled Eulerian and Lagrangian method. J Manuf Process 34:158–166. https://doi.org/10.1016/j.jmapro.2018.05.022
5. Salloomi KN (2019) Fully coupled thermomechanical simulation of friction stir welding of aluminum 6061-T6 alloy T-joint. J Manuf Process 45:746–754. https://doi.org/10.1016/j.jmapro.2019.06.030
6. Lorrain O, Serri J, Favier V et al (2009) A contribution to a critical review of friction stir welding numerical simulation. J Mech Mater Struct 4:351–369. https://doi.org/10.2140/jomms.2009.4.351
7. Zhang Z, Zhang HW (2014) Solid mechanics-based Eulerian model of friction stir welding. Int J Adv Manuf Technol 72:1647–1653. https://doi.org/10.1007/s00170-014-5789-4
8. Mandal S, Rice J, Elmustafa AA (2008) Experimental and numerical investigation of the plunge stage in friction stir welding. J Mater Process Technol 203:411–419. https://doi.org/10.1016/j.jmatprotec.2007.10.067
9. Meyghani B, Wu C (2020) Progress in thermomechanical analysis of friction stir welding. Chin J Mech Eng 33:12. https://doi.org/10.1186/s10033-020-0434-7
10. Wang X, Gao Y, McDonnell M, Feng Z (2020) On the solid-state-bonding mechanism in friction stir welding. Extreme Mech Lett 37:100727. https://doi.org/10.1016/j.eml.2020.100727
11. Ansari MA, Samanta A, Behnagh RA, Ding H (2019) An efficient coupled Eulerian–Lagrangian finite element model for friction stir processing. Int J Adv Manuf Technol 101:1495–1508. https://doi.org/10.1007/s00170-018-3000-z
12. Zhu Z, Wang M, Zhang H et al (2017) A finite element model to simulate defect formation during friction stir welding. Metals 7:256. https://doi.org/10.3390/met7070256
13. Al-Badour F, Merah N, Shuaib A, Bazoune A (2013) Coupled Eulerian Lagrangian finite element modeling of friction stir welding processes. J Mater Process Technol 213:1433–1439. https://doi.org/10.1016/j.jmatprotec.2013.02.014
14. Ducobu F, Arrazola P-J, Rivière-Lorphèvre E et al (2017) The CEL method as an alternative to the current modelling approaches for Ti6Al4V orthogonal cutting simulation. Procedia CIRP 58:245–250. https://doi.org/10.1016/j.procir.2017.03.188
15. ABAQUS Version 6.6 Documentation. https://classes.engineering.wustl.edu/2009/spring/mase5513/abaqus/docs/v6.6/index.html. Accessed 15 Dec 2020
16. Feng F, Huang S, Meng Z et al (2014) A constitutive and fracture model for AZ31B magnesium alloy in the tensile state. Mater Sci Eng A 594:334–343. https://doi.org/10.1016/j.msea.2013.11.008
17. Ulacia I, Salisbury CP, Hurtado I, Worswick MJ (2011) Tensile characterization and constitutive modeling of AZ31B magnesium alloy sheet over wide range of strain rates and temperatures. J Mater Process Technol 211:830–839. https://doi.org/10.1016/j.jmatprotec.2010.09.010
18. Veljic D, Milenko P, Sedmak A, Rakin M (2011) Numerical simulation of the plunge stage in friction stir welding alloys EN AW 2024 T 351 and EN AW 7049A T 652. J Technol Plast 36:2. https://doi.org/10.2478/v10211-011-0010-3
19. Yu M, Li WY, Li JL, Chao YJ (2012) Modelling of entire friction stir welding process by explicit finite element method. Mater Sci Technol 28:812–817. https://doi.org/10.1179/1743284711Y.0000000087
20. El-Sayed MM, Shash AY, Mahmoud TS, Rabbou MA (2018) Effect of friction stir welding parameters on the peak temperature and the mechanical properties of aluminum alloy 5083-O. In: Öchsner A, Altenbach H (eds) Improved performance of materials. Springer International Publishing, Cham, pp 11–25
21. Frigaard Ø, Grong Ø, Midling OT (2001) A process model for friction stir welding of age hardening aluminum alloys. Metall Mater Trans A 32:1189–1200. https://doi.org/10.1007/s11661-001-0128-4
22. Mishra RS, De PS, Kumar N (2014) Fundamentals of the friction stir process. In: Mishra RS, Ma ZY (eds) Friction stir welding and processing. Springer International Publishing, Cham, pp 13–58. https://doi.org/10.1007/978-3-319-07043-8_2

23. Hadadzadeh A, Wells MA (2013) Mathematical modeling of thermo-mechanical behavior of strip during twin roll casting of an AZ31 magnesium alloy. J Magn Alloys 1:101–114. https://doi.org/10.1016/j.jma.2013.04.001

24. Hao H, Maijer DM, Wells MA et al (2010) Modeling the stress–strain behavior and hot tearing during direct chill casting of an AZ31 magnesium billet. Metall Mater Trans A 41:2067–2077. https://doi.org/10.1007/s11661-010-0216-4

25. Serindag HT, Kiral BG (2017) Friction stir welding of AZ31 magnesium alloys—a numerical and experimental study. Lat Am J Solids Struct 14:113–130. https://doi.org/10.1590/1679-78253162

26. Gao E, Zhang X, Liu C, Ma Z (2018) Numerical simulations on material flow behaviors in whole process of friction stir welding. Trans Nonferr Met Soc China 28:2324–2334. https://doi.org/10.1016/S1003-6326(18)64877-0

27. Aziz SB, Dewan MW, Huggett DJ et al (2018) A fully coupled thermomechanical model of friction stir welding (FSW) and numerical studies on process parameters of lightweight aluminum alloy joints. Acta Metall Sin Engl Lett 31:1–18. https://doi.org/10.1007/s40195-017-0658-4

28. Khosa SU, Weinberger T, Enzinger N (2010) Thermo-mechanical investigations during friction stir spot welding (FSSW) of AA6082-T6. Weld World 54:R134–R146. https://doi.org/10.1007/BF03263499

29. Li W, Yu M, Li J (2010) Effects of mass scaling factor on the plunge stage of friction stir welding. Hanjie XuebaoTrans China Weld Inst 31:1–4

30. Hammelmüller F, Zehetner C (2015) Increasing numerical efficiency in coupled Eulerian–Lagrangian metal forming simulations. In: A: COMPLAS XIII. "COMPLAS XIII: proceedings of the XIII international conference on computational plasticity: fundamentals and applications". CIMNE edition. CIMNE, Barcelona, pp 727–733

31. Figueiredo RB, Langdon TG (2019) Processing magnesium and its alloys by high-pressure torsion: an overview. Adv Eng Mater 21:1801039. https://doi.org/10.1002/adem.201801039

32. Padmanaban G, Balasubramanian V (2010) An experimental investigation on friction stir welding of AZ31B magnesium alloy. Int J Adv Manuf Technol 49:111–121. https://doi.org/10.1007/s00170-009-2368-1

33. Padhy GK, Wu CS, Gao S (2018) Friction stir based welding and processing technologies—processes, parameters, microstructures and applications: A review. J Mater Sci Technol 34:1–38. https://doi.org/10.1016/j.jmst.2017.11.029

34. Asadi P, Kazemi-Choobi K, Elhami A (2012) Welding of magnesium alloys. In: Monteiro WA (ed) New features on magnesium alloys. InTech, Houston

35. Padmanaban G, Balasubramanian V (2009) Selection of FSW tool pin profile, shoulder diameter and material for joining AZ31B magnesium alloy—an experimental approach. Mater Des 30:2647–2656. https://doi.org/10.1016/j.matdes.2008.10.021

36. Suhuddin UFHR, Mironov S, Sato YS et al (2009) Grain structure evolution during friction-stir welding of AZ31 magnesium alloy. Acta Mater 57:5406–5418. https://doi.org/10.1016/j.actamat.2009.07.041

37. Mironov S, Sato YS, Kokawa H (2019) Influence of welding temperature on material flow during friction stir welding of AZ31 magnesium alloy. Metall Mater Trans A 50:2798–2806. https://doi.org/10.1007/s11661-019-05194-0

38. Rai R, De A, Bhadeshia HKDH, DebRoy T (2011) Review: friction stir welding tools. Sci Technol Weld Join 16:325–342. https://doi.org/10.1179/1362171811Y.0000000023

39. Singh BR (2012) A hand book on friction stir welding. LAP Lambert Academic Publishing, London